



Ni catalysts with La as promoter supported over Y- and BETA- zeolites for CO₂ methanation

Adrián Quindimil, Unai De-La-Torre, Beñat Pereda-Ayo, José A. González-Marcos, Juan R. González-Velasco*

Departamento de Ingeniería Química, Facultad de Ciencia y Tecnología, Universidad del País Vasco UPV/EHU, Barrio Sarriena, 48940, Leioa, Bizkaia, Spain

ARTICLE INFO

Keywords:

Y-zeolite
BETA-zeolite
Zeolite-supported Ni catalysts
La promoter
CO₂ methanation

ABSTRACT

The hydrogenation of CO₂ into methane is considered a plausible process to storage renewable energy in form of methane and reducing CO₂ anthropogenic emissions. Microporous solids such as zeolites have been scarcely studied yet for this application. This study aims to evaluate and compare the catalytic performance of zeolite (Y and BETA) supported Ni catalysts for CO₂ methanation. The physicochemical properties of the prepared catalysts were characterized by XRD, BET, CO₂-TPD, H₂-TPR and XPS, and CO₂ methanation was carried out in a tubular reactor at conditions of H₂/CO₂ = 4, GHSV = 10,000 h⁻¹ and temperatures from 200 to 500 °C. Neutralization of both zeolites by Na⁺ ion exchange enhanced the CO₂ conversion as weaker CO₂ adsorption sites and reducibility are promoted. BETA resulted in a better support than Y zeolite due to the presence of more easily reducible Ni²⁺, which acts as precursor of active Ni⁰ accessible under reaction conditions. Indeed, the surface basicity and Ni dispersion of Ni/BETA catalysts were considerably promoted by impregnation of different loads of La₂O₃, which increase the amount of CO₂ adsorption sites and even active hydrogenation sites resulting in a significant increase of activity and selectivity towards CH₄. The optimal Ni-10%La₂O₃/Na-BETA formulation resulted in T₅₀ of 320 °C, CO₂ conversion of 65% at 350 °C, with almost total selectivity to CH₄ and maintaining stability for more than 24 h.

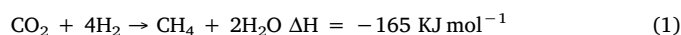
1. Introduction

Anthropogenic CO₂ emissions from an energy system based on fossil fuels are the main cause of climate change. It is estimated that annual CO₂ emissions will continue to increase due to the global growing energy demand linked to the exponential increase in population. In fact, the International Energy Agency (IEA) foresees 35.7 Gt of emitted CO₂ for 2040, a quantity far from enough to avoid severe climate change [1].

The replacement of fossil energy by renewable energy is presented as the better alternative to overcome this environmental challenge. In the near future this carbon-free sustainable energy source is expected to play an important role in a mixed energy system. At present, however, renewable energy sources remain considerably less efficient and therefore less profitable than fossil energy sources. The lower efficiency of renewable energies is due, in part, to their intermittency: wind and solar energy are fluctuating and have to be balanced for electric grid stability purposes. For that reason, there is a growing interest in the development of renewable energy storage forms [2].

Nowadays, the electrical power obtained from wind turbines and solar panels can be stored in form of energy vector such as H₂ or CH₄. Hydrogen has a higher calorific value than methane (33,900 vs. 13,249 kcal kg⁻¹) and no CO₂ is formed during H₂ combustion. However, hydrogen also presents some drawbacks compared to methane: (i) very low density, thus its storage is considerably more expensive and (ii) infeasibility of large-scale transport due to incompatibility of the current gas grid. Thus, the conversion of renewable energy into methane seems to be by now a more suitable technology.

Valorization of CO₂ by hydrogenation is a promising alternative, not only because of the use of renewable energy, but also because CO₂ anthropogenic emissions are reduced. Carbon dioxide from flue gas can be combined with H₂ generated from renewable energies and converted catalytically into methane or synthetic natural gas (SNG), according to the Sabatier reaction:



In fact, as a proof of concept, the e-gas plant of Audi Motor Company located in Werlte (Germany) efficiently produces 1000 tons of

* Corresponding author.

E-mail address: juanra.gonzalezvelasco@ehu.es (J.R. González-Velasco).

<https://doi.org/10.1016/j.apcatb.2018.07.034>

Received 6 April 2018; Received in revised form 3 July 2018; Accepted 9 July 2018

Available online 11 July 2018

0926-3373/© 2018 Elsevier B.V. All rights reserved.

SNG per year, combining renewable hydrogen and concentrated CO₂ from a nearby biogas plant.

CO₂ is relatively difficult to be hydrogenated and indeed more difficult than CO, although simultaneous methanation of CO and CO₂ is frequently encountered in a coexistent system, where reactions between CO and CO₂ methanation are competing. A complete network of possible reactions involved in the methanation of carbon dioxides is proposed in literature [3,4]. On the basis of 10 reactions involved in the system with CO/CO₂/H₂/H₂O as reactants, a systematic thermodynamic equilibrium analysis of the methanation reactions of carbon oxides was reported by Gao et al. [4]. The effects of temperature, pressure, H₂/CO₂ (and H₂/CO) and addition of water steam (and O₂, CH₄ and C₂H₄) on the methanation reactions were comprehensively investigated [4,5].

CO₂ methanation catalysts reported in literature normally consists of an active metal supported on a metal oxide. Ru and Ni have been the most studied metals. On the one hand, ruthenium is the most active and selective metal in CO₂ hydrogenation into methane. The only disadvantage against nickel is the highest cost (more than 500 times, www.infomine.com). On the other hand, nickel seems to be the most active and selective among the non-noble metals, which is widely used in the industry due to its low cost. The main reported disadvantage of Ni-based catalysts versus those based on Ru is deactivation due to interaction with CO and formation of mobile nickel carbonyls that result in the metal sintering [6]. Nevertheless, the stability of nickel can be improved by addition of promoters [7].

Concerning the support, mesoporous solids are usually used, such as Al₂O₃ [8], SiO₂ [9], TiO₂ [10], ZrO₂ [11], CeO₂ [12] and Ce-Zr mixed oxides [13]. On the contrary, microporous solids as catalytic supports for CO₂ methanation have been scarcely studied in the literature for CO₂ methanation, e.g. Y zeolite supported Ni catalysts [14–16]. The main disadvantage of protonic zeolites is their small capacity to adsorb CO₂. However, acidity of zeolites can easily be neutralized by alkali ion exchange (as Na⁺ or K⁺), which are known to improve CO₂ adsorption capacity [17–19]. In addition, due to their high specific surface area, it is possible to modulate surface basicity by the impregnation of great loadings of CO₂ adsorbents such as alkaline earth metals (e.g. Ca²⁺, Mg²⁺, Ba²⁺) and rare earth metals (e.g. La₂O₃, CeO₂, Pr₂O₃). As far as we know, BETA type zeolite has not been studied for this application. Therefore, this work is aimed to prepare, characterize and compare the catalytic performance of protonic or Na-exchanged Y and BETA zeolite supported Ni catalysts. Additionally, the effect of La₂O₃ as a CO₂ adsorption promoter for the catalytic activity is investigated.

2. Experimental

2.1. Catalysts preparation

The synthesized samples consisted of zeolite supported Ni catalysts, some of them promoted by La. On the one hand, three types of zeolites were used as a support supplied by Zeolyst International: CBV100 (Na-Y, Si/Al = 2.6), CBV400 (H-Y, Si/Al = 2.6) and CP814E (NH₄-BETA, Si/Al 12.5). From NH₄-BETA, zeolite H-BETA and Na-BETA were synthesized as follows. The protonic form of BETA zeolite was obtained by simple calcination at 550 °C for 4 h with a heating rate of 1 °C min⁻¹. The Na-BETA zeolite was prepared by the metal ion exchange procedure: the required amount of NaNO₃ (Merck, 99.5%) was dissolved in deionized water (0.5 M solution); then, NH₄-BETA was added to this solution (10 mL/g) and the suspension was continuously stirred for 24 h at room temperature. During the preparation pH = 7 was kept by the addition of ammonia. After the ion exchange, the support was filtered, washed twice with deionized water and dried at 110 °C overnight. This procedure was repeated twice and finally the exchanged zeolite was calcined for 4 h at 550 °C with a heating rate of 1 °C min⁻¹.

On the other hand, the incipient wetness impregnation procedure was used for preparing Ni/zeolite catalysts. This method consisted in

Table 1

Nomenclature and chemical composition of the prepared catalysts.

Catalyst label	Framework	Si/Al ^a	Na (wt. %) ^a	Ni (wt. %) ^a	La ₂ O ₃ (wt. %) ^a
Ni/H-Y	FAU	2.5	1.4	9.5	–
Ni/Na-Y	FAU	2.6	6.0	9.9	–
Ni/H-BETA	BEA	12.4	0.0	9.2	–
Ni/Na-BETA	BEA	11.9	1.4	9.5	–
Ni-5La ₂ O ₃ /Na-BETA	BEA	12.2	1.4	9.6	3.2
Ni-10La ₂ O ₃ /Na-BETA	BEA	12.7	1.3	7.8	7.4
Ni-15La ₂ O ₃ /Na-BETA	BEA	12.3	1.2	7.3	12.0

^a Determined by XRF.

adding the Ni(NO₃)₂ solution (Sigma Aldrich, 99.99%) dropwise to zeolite support so that the solute was driven into pores by capillary forces. Once an excess of solution is achieved, the mass transfer into the pores shifts to diffusion instead of capillary forces (slower process). In all cases, the nominal content of nickel was set at 10% and, after impregnation, the catalysts were calcined at 550 °C for 6 h with a heating rate of 5 °C min⁻¹. On the other hand, 5, 10 and 15% La₂O₃ promoted catalysts were prepared by successive impregnations in LaNO₃·6H₂O (Sigma Aldrich, 99.0%) and NiNO₃·6H₂O solutions. In total, 7 catalysts were prepared and nominated as in Table 1, where the framework type, chemical composition and Si/Al ratios are shown.

2.2. Characterization techniques

X Ray Diffraction (XRD). Crystallinity of the powder catalysts was measured by XRD on a PANalytical Xpert PRO diffractometer with Cu Kα radiation (λ = 1.5418 Å) and Ni filter. The operating conditions were 40 kV and 40 mA and diffractograms were recorded from 5 to 70° 2 θ with 0.02° per second sampling interval. PANalytical X'pert HighScore specific software was used for data treatment and JCPDS database was used to interpret the diffractograms.

N₂ physisorption. Textural properties of the samples were determined from N₂ adsorption-desorption isotherms measured at 77 K using a Micromeritics TRISTAR II 3020 equipment. The specific surface areas of microporous samples were calculated by complete BET equation which assumes a defined number of nitrogen layers and positive values of C parameter. Pore volumes were calculated by t-plot method and pore size distribution of only mesoporous solids was determined using BJH method. The samples were previously degassed overnight under N₂ flow.

Diffuse Reflectance UV–vis. The oxidation states and the coordination of Ni species were evaluated by DR UV–vis spectroscopy. UV–vis-NIR measurements were carried out in a Varian Cary 5000 apparatus coupled to a Diffuse Reflectance Internal 2500. The polycrystalline samples were finely grinded and the spectra were recorded at room temperature in a range of wave number among 200 and 2500 nm.

Hydrogen Temperature Programmed Reduction (H₂-TPR). The reducibility of the Ni/zeolite catalysts was determined by TPR. The experiments were carried out on a Micromeritics AutoChem 2920 instrument. Firstly, samples were pre-treated at 250 °C or 500 °C for 30 min under Ar or 5%O₂/He flow in order to remove adsorbed or chemisorbed H₂O and CO₂, respectively. The pre-treatment temperature of 500 °C was used for catalysts with La₂O₃. The reducing gas flow was 50 mL·min⁻¹ of 5%H₂/Ar and the temperature was raised from 40 to 900 °C with a heating rate of 10 °C min⁻¹. The water formed during reduction was trapped using a cold trap and the hydrogen consumption was continuously monitored with a TCD detector.

CO₂ Temperature Programmed Desorption (CO₂-TPD). Total basicity and basic strength distribution were evaluated by TPD-MS studies. Micromeritics AutoChem 2920 instrument was used coupled to a MKS

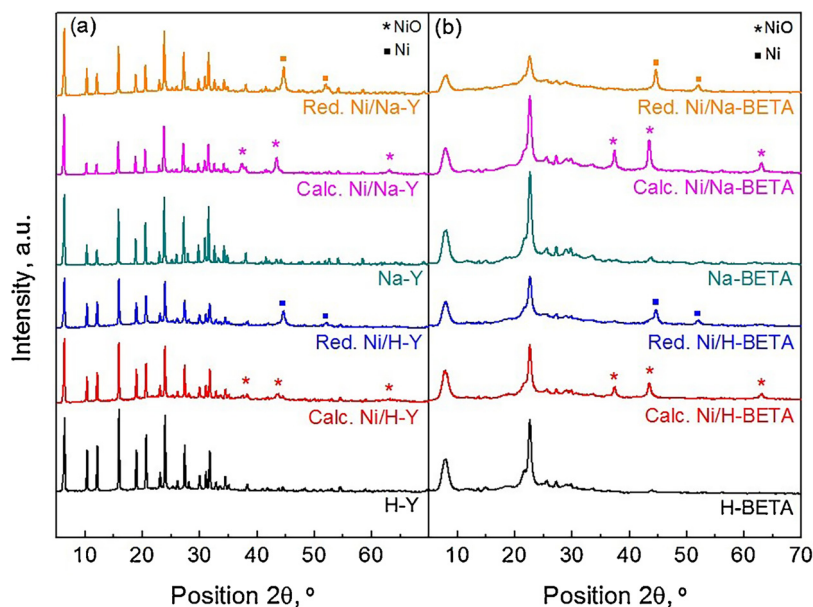


Fig. 1. XRD patterns of (a) Y-zeolite supported catalysts (calcined and reduced) and (b) BETA-zeolite supported catalysts (calcined and reduced).

Cirrus mass spectrometer. Samples were pre-treated at 500 °C for 60 min under He flow and then cooled down to 50 °C. Then, CO₂ adsorption step was performed by feeding 50 cm³ min⁻¹ of 5%CO₂/He flow until saturation. Subsequently, the samples were flushed out with helium for 60 min to remove physisorbed CO₂ from the surface. Finally, desorption was carried out from 50 to 850 °C with a heating rate of 10 °C min⁻¹. The CO₂ desorption was continuously monitored with the mass spectrometer.

Transmission Electron Microscopy (TEM-STEM). TEM measurements were carried out at FEI Titan Cubed G2 60–300 electron microscope at 200 kV equipped with a high-brightness X-FEG Schottky field emission electron gun, a monochromator, CEOS GmbH spherical aberration (Cs) corrector on the image side and a Super-X EDX system under high annular dark field (HAADF) detector for Z contrast imaging in STEM conditions (camera length of 185 mm). The nominal size of the electron probe used for STEM and EDX maps was 0.5 nm and the probe current 170 pA and the semiconvergence angle was 14 mrad. High-angle annular dark-field HAADF STEM images were collected with an inner detector radius of 63.5 mrad. The samples for the TEM were prepared by dispersion into ethanol solvent and keeping the suspension in an ultrasonic bath for 15 min, after a drop of suspension was spread onto a TEM copper grid (300 Mesh) covered by a holey carbon film followed by drying under vacuum.

2.3. CO₂ methanation experiments

CO₂ methanation reaction were performed in a downflow fixed bed reactor ($D_{in} = 9$ mm) and the product distribution was analyzed with a gas chromatograph (Agilent 7890 B). The catalysts were pre-treated at 500 °C for 1 h under 20%H₂/He flow (250 cm³ min⁻¹) and after cooling down to 200 °C in inert gas, the reaction mixture was fed to the reactor with a 4:1:1.25 H₂:CO₂:He molar relation. The reaction temperature range explored was from 200 to 500 °C in steps of 25 °C. The He, H₂, CO₂, CH₄ and CO concentrations at the reactor exit at every temperature were monitored once steady state was reached. He, H₂, CH₄ and CO were followed by MolSieve type columns, whereas CO₂ was followed by HayeSep type column.

The experiments were carried out at atmospheric pressure with 0.5 g of catalysts, which were pelletized, grinded and sieved to obtain particles size 0.3–0.5 mm. The catalyst particles were diluted to 50% with quartz particles in order to improve mass and heat transfer. Under

these conditions, GHSV and W/F_{A0} resulted in 10,000 h⁻¹ and 4.67 g h·mol⁻¹ respectively. CO₂ conversion (X_{CO_2}) and CH₄ (Y_{CH_4}) yield were calculated as:

$$X_{CO_2} = \frac{F_{CO_2}^{in} - F_{CO_2}^{out}}{F_{CO_2}^{in}} \times 100 \quad (2)$$

while selectivities towards CH₄ (S_{CH_4}) and CO (S_{CO}) were calculated as:

$$S_{CH_4} = \frac{F_{CH_4}^{out}}{F_{CO_2}^{in} - F_{CO_2}^{out}} \times 100 \quad (3)$$

$$S_{CO} = \frac{F_{CO}^{out}}{F_{CO_2}^{in} - F_{CO_2}^{out}} \times 100 \quad (4)$$

Also yields of CO₂ to CH₄ and CO can be determined as:

$$Y_{CH_4} = \frac{F_{CH_4}^{out}}{F_{CO_2}^{in}} \times 100 = S_{CH_4} \times X_{CO_2} \quad (5)$$

$$Y_{CO} = \frac{F_{CO}^{out}}{F_{CO_2}^{in}} \times 100 = S_{CO} \times X_{CO_2} \quad (6)$$

Finally, T_{50} parameter is defined as the temperature at which 50% of CO₂ is converted.

3. Results and discussion

3.1. Ni/zeolite catalysts

3.1.1. Characterization

Fig. 1 shows XRD patterns of the protonic zeolites (H-Y and H-BETA, Fig. 1a and b, respectively) as well as of those exchanged with Na⁺. It can be observed that the diffractogram of Na-BETA zeolite is almost identical to its counterpart, which means that the crystalline nature of the zeolite was not modified after the incorporation of Na⁺. However, minor loss of crystallinity can be detected when Na⁺ is incorporated in Y zeolite, as already revealed other authors [19,20]. Also, no Na₂O was detected in XRD spectra, assuring a successful exchange of Na⁺ in both zeolites. After Ni impregnation, new diffraction peaks at 37.3, 43.3 and 62.9° 2θ revealed the formation of NiO (bunsenite phase) in the impregnated samples [6] which are marked with asterisks. As expected, the presence of elemental nickel instead of NiO was detected for the samples reduced at 500 °C for 1 h under 20%H₂/He, as revealed by XRD

Table 2
Physico-chemical properties of supports and Ni catalysts.

Sample	τ_{Ni} (nm) ^a	S_{BET} (m ² ·g ⁻¹) ^b	V_{micro} (cm ³ ·g ⁻¹) ^c	V_{meso} (cm ³ ·g ⁻¹) ^c	Reducible Ni ²⁺ at 500 °C (%) ^d
H-Y	–	720.5	0.24	0.07	–
Ni/H-Y	17.0	621.1	0.20	0.10	43
Na-Y	–	832.1	0.29	0.02	–
Ni/Na-Y	19.8	665.9	0.22	0.05	91
H-BETA	–	587.3	0.17	0.60	–
Ni/H-BETA	19.1	485.3	0.12	0.38	95
Na-BETA	–	513.6	0.13	0.38	–
Ni/Na-BETA	20.1	415.7	0.10	0.32	98

^a Estimated by Scherrer equation.

^b Calculated by complete BET equation.

^c Determined by application of t-Plot method.

^d Calculated from H₂-TPR profiles. Reduction conditions: 500 °C for 1 h with 20% H₂/He.

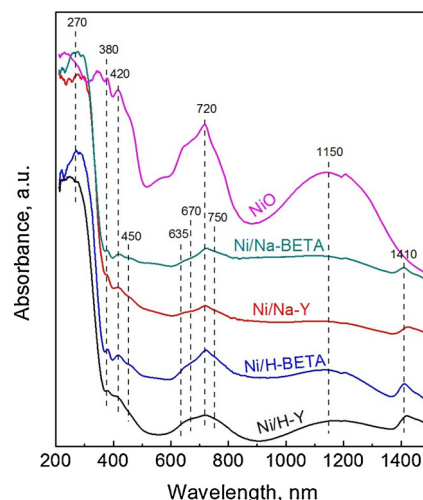


Fig. 2. UV-vis-NIR spectra of Ni/zeolite catalysts.

peaks at 44.3 and 51.7° 2 θ marked with squares [8].

The Ni crystallite sizes, estimated by the Scherrer equation, are displayed in Table 2. A smaller crystallite size can be observed for Ni/H-Y catalyst when comparing to Ni/H-BETA catalyst, which is related to differences in zeolitic structure: unlike BEA, FAU structure contains accessible cavities for Ni particles that might result in higher metal dispersion over the outer surface of the zeolite. In the same line, Na⁺ incorporation in BETA zeolite produces the formation of bigger Ni crystallites due to the partial pore blockage, which results in less accessible zeolitic framework [21]. Anyway, no significant differences are observed in the crystallite size, which indicates similar dispersion of the surface Ni for all catalysts.

The N₂ physisorption isotherms of H-Y and H-BETA zeolites are shown in Fig. S1. In the case of H-Y zeolite the shape of the isotherms is characteristic of a microporous solid: great amount of N₂ is adsorbed at very low pressures by micropore filling and thereafter very little adsorption takes place (isotherm type I according to IUPAC). However, a different isotherm shape is observed for H-BETA zeolite: although a great amount of N₂ is adsorbed at very low relative pressures, more N₂ is also adsorbed at intermediate pressures by multilayer filling (isotherm type IV). The appearance of a hysteresis loop at relative pressures up to 0.65 for H-BETA indicates the presence of mesoporous which are suitable for impregnation of high metal loadings.

Textural properties of the prepared samples are also shown in Table 2. Regardless the presence of Na⁺ and after Ni impregnation over H-Y and Na-Y zeolites, a notable decrease of specific surface area (14 and 20%) and micropore volume (17 and 24%) is produced due to the formation of NiO clusters that block the zeolite pores, which reduces the adsorption capacity of the supports [22,23]. On the other hand, a similar trend can be observed in the textural properties of BETA zeolite after Ni addition, resulting in BET surface reduction of 17 and 19% for H-BETA and Na-BETA, respectively. Additionally, a notorious decrease of both microporous and mesoporous volume is observed. The highest reduction is seen when Ni is impregnated over H-BETA, being microporous and mesoporous volume reduced a 29% and 37%, respectively.

In order to determine the symmetry and the coordination of nickel species dispersed on the zeolites, diffuse reflectance spectroscopy was carried out. Fig. 2 shows UV-vis-NIR spectra of Y and BETA zeolites after Ni impregnation. In the UV-vis region (from 200 to 800 nm), all catalysts present bands centered at 270, 380, 420 and 720 nm, all of them characteristics of NiO species. The band centered at the lowest wavelength is assigned to O²⁻ → Ni²⁺ metal to ligand charge transfer, while the bands at intermediate and high wavelengths are assigned to d-d electron transitions of Ni²⁺ in octahedral coordination inside NiO [23]. In addition, two bands centered at 450 and 635 nm can be distinguished which correspond to d-d electron transitions of Ni²⁺

exchanged in tetrahedral coordination inside zeolite framework [24–26]. The green Ni/H-Y catalyst also presents bands at 670 and 750 nm, not so clearly detected in other samples and which are assigned to d-d electron transition of Ni²⁺ ions in octahedral coordination [21,27,28]. However, the presence of this Ni species cannot be disregarded for the latter samples.

On the other hand, other two bands can be observed in the NIR domain (from 800 to 2500 nm). The wide band centered at 1150 nm is attributed to the ν_1 (³A_{2g} → ³T_{2g}) transition of octahedrally coordinated Ni²⁺ and appears in all spectra of prepared samples indicating the presence of NiO. In contrast, the last band centered at 1410 nm is related to vibrations of surface hydroxyl groups of zeolite supports [29] and, as expected, is less intense for Ni/Na-zeolite catalysts than for Ni/H-zeolite catalysts.

The redox properties of the prepared samples were examined by H₂-TPR technique in order to analyze the reducibility of different nickel species dispersed on each zeolite. Fig. 3a and b show the H₂-TPR runs for Ni/Y and Ni/BETA catalysts, respectively. In line with UV-vis-NIR results, the appearance of several peaks in TPR spectra indicates the

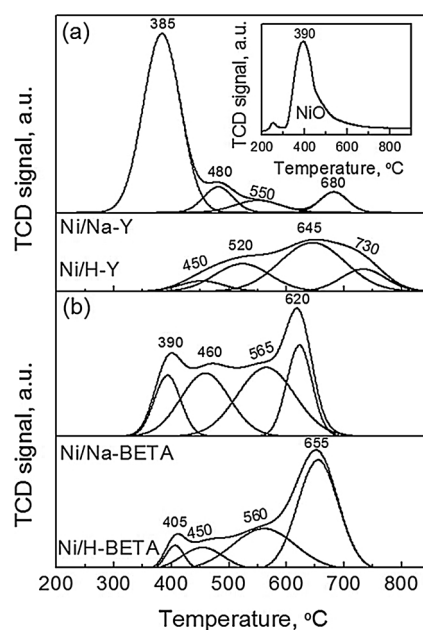


Fig. 3. TPR profiles of (a) Y-zeolite (protonic and sodium) supported Ni catalysts and (b) BETA-zeolite (protonic and sodium) supported Ni catalysts.

presence of various Ni species with different reducibility. On the one hand, four defined H_2 consumption peaks can be observed for Ni/H-Y catalyst (Fig. 3a). The peak at lowest temperature (450 °C) can be attributed to reduction of surface NiO particles interacting with the zeolitic support, whereas peaks located at 520 and 645 °C are attributed to reduction of tetrahedrally coordinated Ni^{2+} species located on supercages and sodalite cages, respectively [22,27,28,30,31]. The peak at highest temperature, with a maximum at 730 °C, is related to reduction of octahedrally coordinated Ni^{2+} exchanged in hexagonal prisms, as was confirmed by UV-vis. On the other hand, a new peak can be distinguished at 385 °C for Ni/Na-Y catalyst. The position of this reduction peak is similar to the observed in the nickel oxide sample (insight Fig. 3a), so it is associated with reduction of NiO particles weakly interacting with Na-Y zeolite and located in the external surface. The shift to lower temperature of H_2 -TPR profile reveals that Ni/Na-Y is a more easily reducible catalyst than Ni/H-Y catalyst. This fact is related to the donation of electrons from Na^+ to nickel [21].

Focusing on BETA supported catalysts (Fig. 3b), unlike zeolite H-Y, BETA zeolite is not formed by cavities: its structure consists of a three-dimensional system of channels, so nickel location is different to that observed in the zeolite Y. For Ni/BETA catalysts four H_2 reduction peaks are also observed. The peaks at lowest temperatures, with maximums located close to 400 and 450 °C, are related to reduction of NiO with different interaction degree with the support. The first peak at the lowest temperature is attributed to reduction of NiO placed on the outer surface while the second peak is assigned to reduction of certain population of NiO clusters with smaller size and higher interaction with the support [23,32,33]. In contrast, peaks at highest temperatures indicate the presence of Ni^{2+} located at different sites: the peak centered around 560 °C is related to reduction of pseudo-tetrahedral Ni^{2+} , whereas the peak located between 620 and 655 °C is related to Ni^{2+} in hexagonal prisms [25,26,34–36]. In line with Y zeolite based catalysts, shift of TPR profile to lower temperatures can be observed in Ni/Na-BETA due to the above mentioned effect.

With the aim of quantifying the amount of Ni^{2+} reducible at temperatures below 500 °C, additional TPR tests of reduced samples were carried out (Fig. S2). The pre-reduction was done under the same conditions used for the reductions prior to the activity tests: 500 °C for 1 h with 20% H_2 /He. As expected, TPR profiles of all catalysts exhibited a single H_2 consumption peak between 600 and 700 °C, which is associated with reduction of exchanged nickel. The amount of reduced nickel during pre-reduction process is quantified in the last column of Table 2. Note that the percentage of reducible Ni^{2+} is above 90% for all catalysts, except for Ni/H-Y (43%), which showed a notable peak at 680 °C. This means that almost all nickel is getting reduced during activity tests for Ni/Na-Y, Ni/H-BETA and Ni/Na-BETA catalysts. Finally, it is worth to mention that calculated H_2/NiO ratios are between 0.9 and 1.1 for all the prepared catalysts, i.e., Ni^{2+} is the only reducible specie.

3.1.2. CO_2 methanation tests

The performances of the prepared catalysts were evaluated by analyzing the obtained CO_2 conversions and CH_4 yields. It must be noted that, in all cases, CO was the only secondary product and that the carbon balance closed within $\pm 5\%$. First, Fig. 4 compares the catalytic activity at increasing temperatures of protonic and sodium zeolites containing Ni. As a general trend, it can be clearly noticed that the presence of exchanged Na^+ in both zeolitic frameworks leads to greater CO_2 conversions in the range of studied temperatures. This effect is more pronounced for Y zeolite supported samples. In fact, the light-off T_{50} curve of Ni/Na-Y catalyst shifts 30 °C to lower temperatures, while light-off curve of Ni/Na-BETA catalyst is only shifted 15 °C. The greater activity of these catalysts, as already explained in H_2 -TPR section (Fig. 3), is not only in line with the reducibility enhancement but also with the presence of weak CO_2 adsorption sites in Na-based catalysts. According to previous studies, the interaction between CO_2 and the

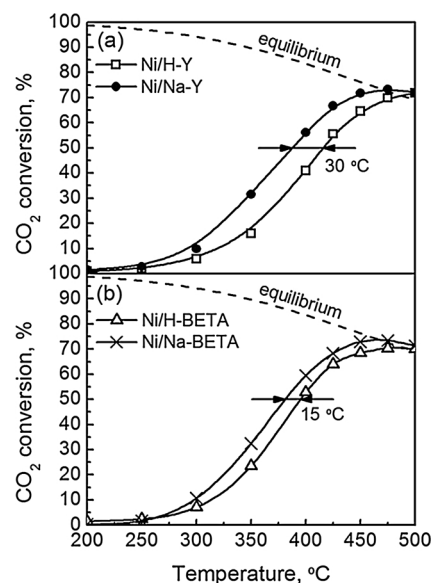


Fig. 4. Effect of temperature on CO_2 conversion for (a) Y-zeolite (protonic and sodium) supported catalysts and (b) BETA-zeolite (protonic and sodium) supported catalysts.

support is improved by the presence of the alkali metal, resulting in a promoted CO_2 activation [21].

By comparing CO_2 conversions of Na^+ free catalysts, greater activity is found for the Ni/H-BETA catalyst. On the one hand, Ni/H-Y sample ($T_{50} = 415$ °C) contains more internally located Ni species providing higher metal dispersion; however, Ni/H-BETA ($T_{50} = 393$ °C) sample presents a greater amount of reducible Ni species at 500 °C (95% vs. 43%) which are considered the active phase for CO_2 methanation [27,37]. Therefore, the higher activity of Ni/H-BETA catalysts could be related to a larger available Ni^0 area during methanation reaction, as revealed H_2 -TPR results shown in Fig. S2.

In contrast, when comparing Na-exchanged supported catalysts, similar CO_2 conversions are observed in all range of studied temperatures. In both cases, 50% of CO_2 conversion occurs around 380 °C and the maximum CO_2 conversions are reached at 450 °C ($X_{CO_2} = 73\%$). Although Ni/Na-Y catalyst has greater reducibility, according to the H_2 -TPR results, Ni/Na-BETA catalyst contains more Ni^{2+} species inside the framework which could provide higher dispersion. Therefore, the same CO_2 methanation activity shown by both catalysts is explained by the presence of similar available surface of active phase during reaction.

C-species distribution at the reactor exit for the prepared catalysts is illustrated in Fig. 5. It can be observed that the highest CH_4 yield is reached at 450 °C, being Na^+ containing catalysts more productive than Ni/H-zeolite catalysts. CO yield, on the contrary, is somewhat lower for Ni/H-zeolite catalysts at 350 °C and somewhat higher at 400 °C. Regardless the reaction temperature, methane yield of the samples reflects the following order: Ni/Na-BETA > Ni/Na-Y > Ni/H-BETA > Ni/H-Y. Thus, Ni/Na-BETA catalyst results in the more active and productive catalyst, showing maximum CO_2 conversion and CH_4 yield values of 73 and 71%, respectively. Indeed, the best catalytic performance of this catalyst is attributed to the enhanced CO_2 adsorption and to the higher dispersion of reducible Ni species.

3.2. Effect of La_2O_3 addition

3.2.1. Characterization

XRD spectra of calcined and reduced Na-BETA supported Ni catalysts after the impregnation of different amounts of La_2O_3 (5, 10 and 15%) are displayed in Fig. 6. XRD spectra of calcined catalysts show peaks at 37.3, 43.3 and 62.9° 2θ , whereas spectra of reduced catalysts

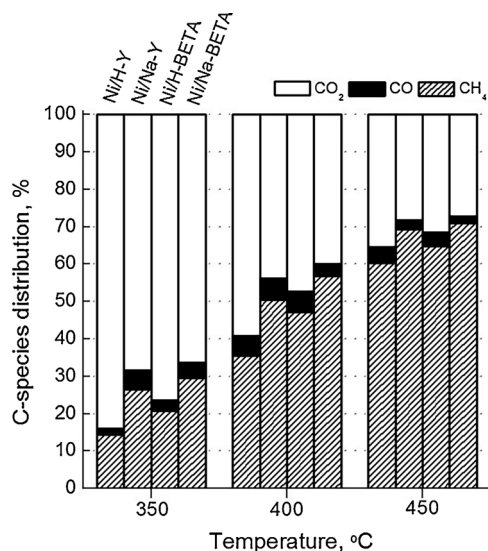


Fig. 5. CO₂ conversion and C-species distribution at the reactor exit for Ni/zeolite catalysts at 350, 400 and 450 °C.

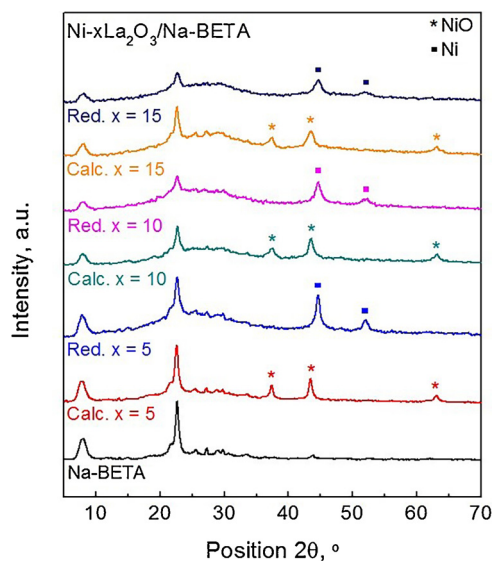


Fig. 6. XRD patterns of calcined and reduced Ni/Na-BETA catalysts with different content of La₂O₃.

show peaks at 44.3 and 51.7° 2θ. The former correspond to NiO (bunsenite phase), while the latter are characteristic of elemental Ni. However, the absence of La₂O₃ characteristic diffraction peaks at 30.0, 39.5 and 46.1° 2θ corresponding to La₂O₃ suggests the formation of an amorphous phase. In fact, the XRD backgrounds of La containing samples are lifted in 25–35° 2θ region with respect to Na-BETA sample, indicating a greater proportion of amorphous material.

Table 3 shows Ni crystallite sizes of La-containing catalysts calculated by the Scherrer equation. It can be noticed that Ni dispersion increases with the addition of La₂O₃ loadings; i.e., the higher the content of La₂O₃, the smaller the Ni crystallite size. In fact, the addition of 15% of La₂O₃ to the Ni/Na-BETA catalyst reduces the surface Ni crystallite size from 20.1 to 7.1 nm, providing higher active phase dispersions, since La₂O₃ acts as a thermal stabilizer of Ni [7,38,39].

N₂ adsorption-desorption isotherms at 77 K of La-containing Ni/Na-BETA catalysts, as well as isotherms of Na-BETA support are included in Figure S3 (Supplementary Material). Similar isotherm shapes are observed in all cases (type I and type IV isotherms combination), suggesting that lanthana addition does not modify considerably the

Table 3

Physico-chemical properties of Ni-La₂O₃/Na-BETA catalysts.

Sample	τ_{Ni} (nm) ^a	S_{EXT} (m ² ·g ⁻¹) ^b	V_{micro} (cm ³ ·g ⁻¹) ^b
Na-BETA	–	224.9	0.13
Ni/Na-BETA	20.1	191.4	0.1
Ni-5La ₂ O ₃ /Na-BETA	12.5	156.8	0.09
Ni-10La ₂ O ₃ /Na-BETA	8.7	142.3	0.08
Ni-15La ₂ O ₃ /Na-BETA	7.1	132.6	0.07

^a Estimated by Scherrer equation.

^b Determined by application of t-Plot method.

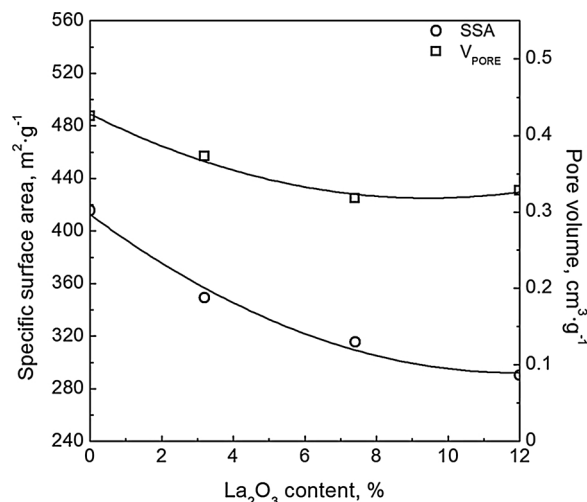


Fig. 7. Effect of lanthana incorporation onto Na-BETA on the specific surface area and pore volume.

textural properties of Na-BETA zeolite.

The external surface areas together with pore volumes are summarized in Table 3. It can be observed that impregnation of increasing loadings of La₂O₃ results in a progressive decrease of the external surface area, which means that impregnated lanthana is located in the outer surface of the zeolite. In fact, external surface area decreases from 224.9 m² g⁻¹ in the Na-BETA catalyst down to 132.6 m² g⁻¹ in the 15% lanthana impregnated catalyst. In the same line, specific surface area also decreases with metal content, as it can be observed in Fig. 7. On the other hand, regarding the pore volume, a similar trend is observed: the higher the metallic load supported on the zeolite, the lower the pore volume, due to a partial blockage of pores [22,23,40]. It is worth to mention that almost no difference can be observed between 15% and 10% La₂O₃ loaded catalysts.

The basicity of different La₂O₃/Na-BETA samples was measured by TPD using CO₂ as probe gas. CO₂-TPD profiles in Fig. 8 show that all these samples contain different CO₂ desorption sites. According to desorption temperature, three different basic sites are detected: weak ($T < 150$ °C), medium ($T = 150$ –550 °C) and strong ($T > 550$ °C) [7,41,42]. For 5%La₂O₃/Na-BETA sample, two peaks centered at 100 and 190 °C are observed, which are attributed to CO₂ desorption from weak (surface OH⁻) and medium (acid-base Lewis pairs) basic sites, whereas samples with 10 and 15% of La₂O₃ present one additional peak centered at 640 °C, which is assigned to bulk carbonate decomposition [43]. However, this strongly attached CO₂ does not participate in the CO₂ methanation, since it is desorbed at temperatures above those of reaction. CO₂ desorption quantification obtained from TPD spectra reveal that lanthana impregnation over Na-BETA results in a considerable increase of the surface basicity due to the formation of new basic sites with different strength. Thus, the higher the La₂O₃ content, the higher the number and strength of basic sites.

The effect of La₂O₃ addition on distribution and reducibility of Ni

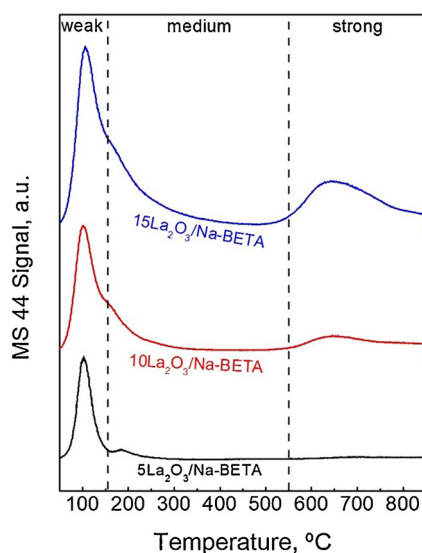


Fig. 8. CO₂-TPD profiles of Na-BETA promoted with different lanthana loadings.

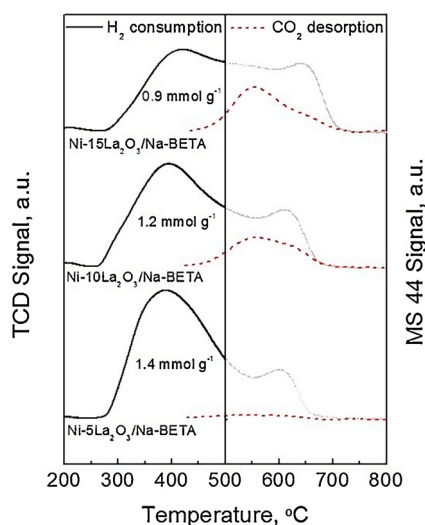


Fig. 9. Evolution of H₂-TPR and the MS 44 signal with temperature for La₂O₃-promoted Ni/Na-BETA catalysts.

species dispersed on the catalysts was determined by H₂-TPR. Before carrying out these experiments, catalysts were degasified for 30 min with 5% O₂/He at 500 °C in order to remove weakly chemisorbed CO₂. Then, H₂ consumption was followed by a TCD detector and, additionally, strongly attached CO₂ desorption was followed by mass spectrometry. The H₂-TPR spectra and CO₂ MS profiles of samples with different lanthana content are shown in Fig. 9. Below 500 °C, a main H₂ consumption peak with a maximum close to 400 °C is observed for all catalysts, which is attributed to reduction of NiO located in the external surface of the zeolite [32,33]. Above 500 °C, in contrast, the growing mass 44 signal (drawn in dashed line) confirms strongly attached CO₂ desorption and hence, the recorded TCD signal cannot be attributed only to H₂ consumption. Nevertheless, the peak appearing above 600 °C is also related to reduction of Ni²⁺ located inside BEA framework [36].

When comparing H₂-TPR profiles of the lanthana based catalysts, a shift to higher temperatures with increasing the La₂O₃ loading is observed. This suggests that the presence of La₂O₃ strengthens the interaction between nickel and the support, due to an increase of the nickel polarization [38,44]. From integration of TPR profiles up to 500 °C, the reducibility of the samples was estimated and reflects this order: Ni/

5La₂O₃/Na-BETA > Ni/10La₂O₃/Na-BETA > Ni/15La₂O₃/Na-BETA. Therefore, the 5% La₂O₃ loaded catalyst presents the highest reducibility. Note that H₂/NiO values are above the stoichiometric ratio, among 1.1 and 1.4, since CO₂ is desorbed during H₂-TPR tests, as demonstrated in Fig. 9.

In order to analyze the nature and surface distribution of La and Ni species, XPS measurements were carried out. Fig. 10a and b show XPS spectra corresponding to Ni 2p and La 3d core levels for fresh and used catalysts, respectively. First, for fresh Ni/Na-BETA catalyst (insight Fig. 10a), Ni 2p_{3/2} region reveals two peaks at ≈ 854.5 and ≈ 857 eV together with a broad shake-up satellite peak at ≈ 862 eV. The main peak at lowest binding energies is attributed to NiO weakly interacting with Na-BETA zeolite, whereas the second one corresponds to the Ni²⁺ cation in exchangeable positions [25,45]. No peak corresponding to reduced nickel (Ni⁰) at ≈ 853 eV was detected. On the other hand, La₂O₃ addition to Ni/Na-BETA catalysts reveals a new main peak in the La 3d_{5/2} region at ≈ 835.7 and a satellite peak at ≈ 838.9 eV. Note that these peaks, assigned to supported La³⁺ [41], intensify with La₂O₃ content, which indicates a progressive increase of the La on the surface. Additionally, a main peak at ≈ 852.4 eV together with its satellite peak at 856.3 are shown in Ni 3d_{3/2} - La 2p_{3/2} region, also corresponding to La³⁺. Regardless the amount of La added in the catalysts, XPS spectra recorded after reaction showed similar binding energies of La³⁺, i.e., La₂O₃ does not suffer from relevant changes after reaction and no Ni⁰ was observed, which indicates that nickel is easily passivated after reaction at ambient temperature [46] (see insight Fig. 10b).

From integration of XPS spectra, surface carbon content as well as Ni/Si and Ni/La atomic ratios of fresh and used Ni-La₂O₃/Na-BETA catalysts were calculated and data is summarized in Table 4. It should be noticed that the content of surface carbon remains similar after reaction in all cases suggesting that no coke was formed during reaction tests. As deduced from Table 4, Ni/Si and La/Si atomic ratios increase with La₂O₃ content, i.e., La₂O₃ addition improves NiO dispersion. This trend is in agreement with XRD results according to which a decrease of NiO crystallite size with La₂O₃ loading was observed. Finally, samples submitted to reaction suffer from a slight decrease of Ni/Si ratio and a small increase of La/Si ratio, probably due to Ni sintering during catalytic tests.

The effect of lanthana on nickel dispersion was also analyzed by transmission electron microscopy. Fig. 11a and d show TEM micrographs of reduced Ni/Na-BETA and Ni-10La₂O₃/Na-BETA catalysts, respectively. Unlike lanthana particles, in those images, Ni particles are clearly observable. Notice that no changes occur in the morphology of nickel particle (spherical) with the impregnation of 10% of La₂O₃. Nevertheless, changes in the particle size distribution are observed (visualized and calculated from at least 100 particles of several TEM images), being the distribution notably narrower for La containing sample. This suggests that lanthana, as structural promoter, controls the growth of nickel particle during calcination. Indeed, smaller Ni particles are observed for Ni-10La₂O₃/Na-BETA, as it presents an average particle size of 10.1 nm (close to the 10.4 nm observed in Table 3 for the same catalyst estimated by Scherrer equation), whereas in Ni/Na-BETA catalyst an average of 17.7 nm can be observed (similar to 20.1 nm presented in Table 2, again estimated by Scherrer equation). Therefore, in agreement with XRD and XPS results, lanthana addition enhances nickel dispersion.

As presence of lanthana was not detectable by TEM, additionally, STEM combined with EDX-elemental mapping was performed. This technique is suitable to differentiate between two or more elements, since provides high resolution element mapping. STEM images together with EDX maps of Ni/Na-BETA and Ni-10La₂O₃/Na-BETA catalysts are displayed in Fig. 11b–c and e–f, respectively. By comparing STEM image and Ni mapping (red colored) of Ni/Na-BETA sample, it is confirmed that Ni is dispersed as spherical particles. Interestingly, EDX map of Ni-10La₂O₃/Na-BETA catalyst shows that La (green colored) is homogeneously dispersed partially covering the surface of the zeolite

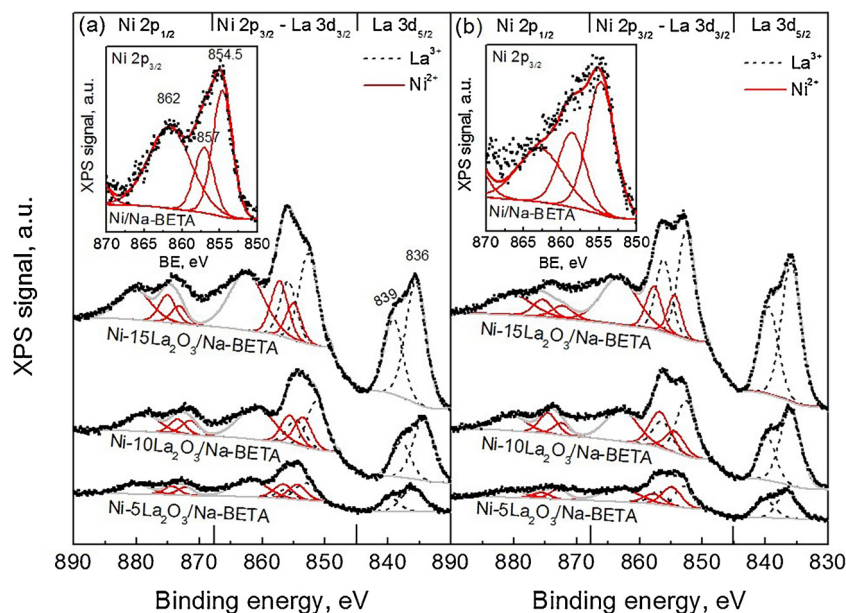


Fig. 10. XPS spectra for La_2O_3 -promoted Ni/Na-BETA catalysts; (a) fresh, (b) after reaction.

Table 4

Surface composition by XPS of the Ni- La_2O_3 /Na-BETA catalysts, before and after reaction.

Catalyst	Before reaction			After reaction		
	C (at. %)	Ni/Si	La/Si	C (at. %)	Ni/Si	La/Si
Ni/Na-BETA	3.0	0.030	–	3.0	0.025	–
Ni-5 La_2O_3 /Na-BETA	2.9	0.035	0.012	3.9	0.031	0.013
Ni-10 La_2O_3 /Na-BETA	2.8	0.068	0.032	2.4	0.067	0.037
Ni-15 La_2O_3 /Na-BETA	3.3	0.110	0.063	2.2	0.086	0.067

and in close contact with nickel. Similar homogeneous dispersion of La_2O_3 supported on Al_2O_3 has already been reported by Z. Boukha et al. [41].

3.2.2. Activity and stability

Fig. 12 shows the effect of La_2O_3 content on CO_2 conversion and the temperature-dependent equilibrium conversion in a dashed line. The onset temperature for CO_2 methanation is 250°C and thermodynamic equilibrium is reached for every catalyst. The required temperatures for $X_{\text{CO}_2} = 50\%$ are 322 , 330 , 334 and 381°C for Ni-10 La_2O_3 , Ni-15 La_2O_3 ,

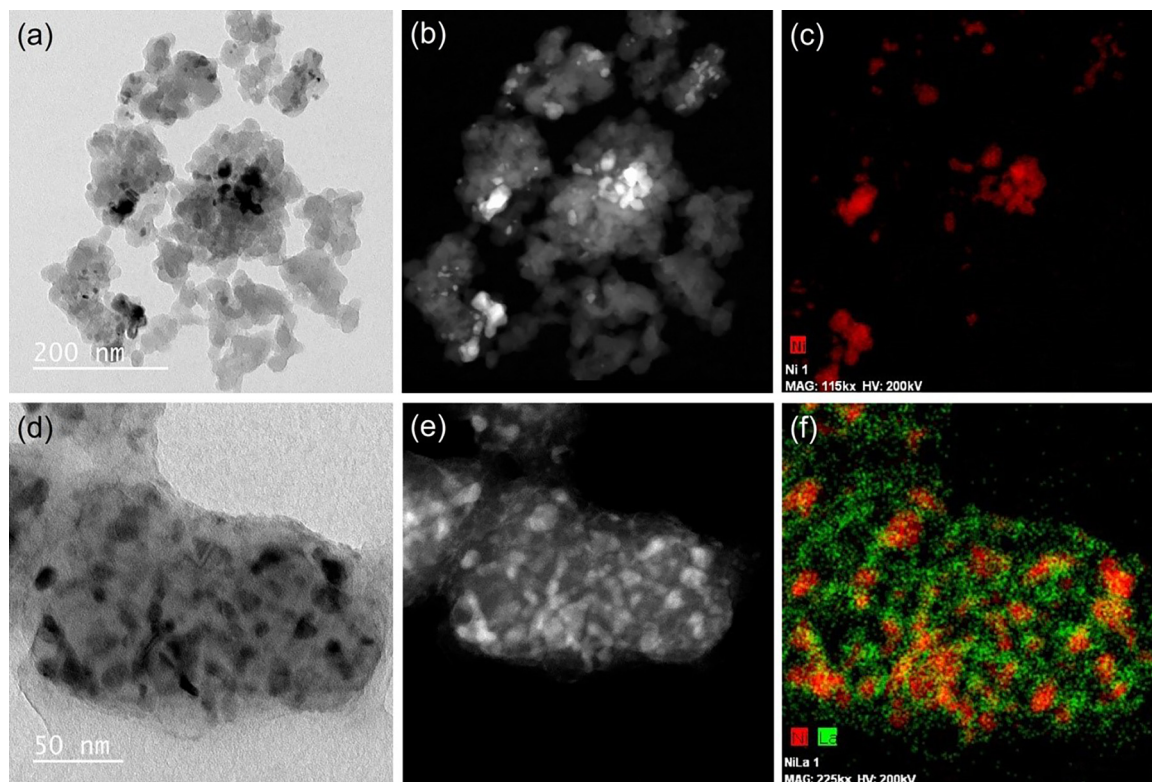


Fig. 11. TEM micrographs (a and d), STEM images (b and e) and EDX maps (c and f) of Ni/Na-BETA and Ni-10 La_2O_3 /Na-BETA catalysts.

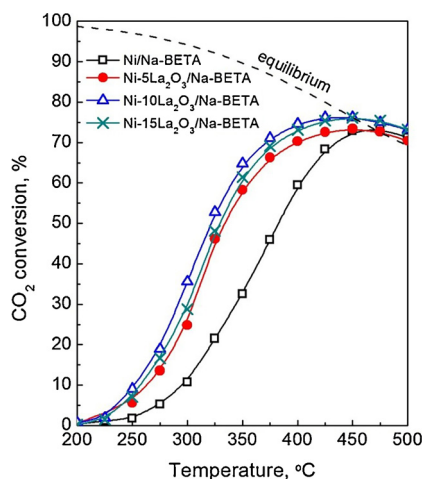


Fig. 12. Light-off curves of La_2O_3 -promoted Ni/Na-BETA catalysts.

Ni-5 La_2O_3 and Ni/Na-BETA catalyst, respectively. The increase in La_2O_3 loading from 5 to 10% leads to higher CO_2 conversions at every temperature, which suggests that the related gain in basicity results in the desired promoter effect. However, although the increase in lanthana nominal content (from 5 to 10%) leads to greater activity, impregnation of La_2O_3 loadings above 10% seems not to be necessary since non enhancement in CO_2 methanation is observed.

According to characterization results, the higher CO_2 methanation activity of Ni-10 La_2O_3 /Na-BETA catalyst in comparison to Ni/Na-BETA catalyst is related to the greater amount of smaller Ni particles (8.7 against 20.1 nm) and to the presence of a considerable amount of weak and medium basic sites (16 vs. $1 \mu\text{mol g}^{-1}$). Also, 10% lanthana loaded catalyst reveals highest reducibility, according to H_2 -TPR results. On the other hand, the slight decrease in catalytic activity observed for Ni-15 La_2O_3 /Na-BETA catalyst is associated with the lower textural properties and reducibility shown in Fig. 9.

In Fig. 13 the C-species distribution at 300, 350 and 400 °C is shown for Ni/Na-BETA and Ni-10 La_2O_3 /Na-BETA catalysts. As in the case of Ni/zeolite catalysts, CO from RWGS was the only detected by-product being the carbon balance closed between 95–105%. It can be observed that CH_4 yield is increased and that CO yield is considerably reduced by addition of 10% of La_2O_3 for all studied temperatures. The greatest difference among product yields occurs at the reaction temperature of

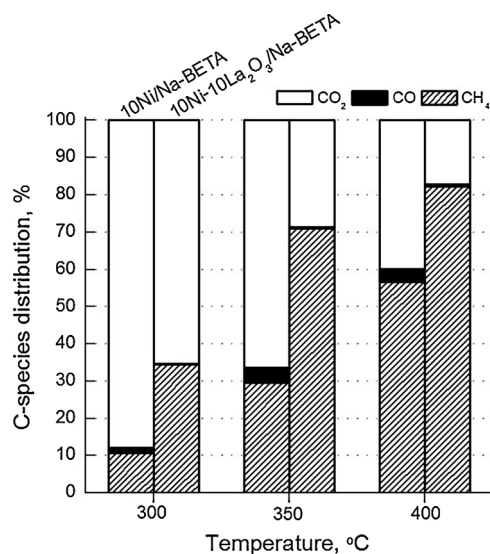


Fig. 13. CO_2 conversion and C-species distribution at the reactor exit for Ni/Na-BETA and Ni-10 La_2O_3 /Na-BETA catalysts at 300, 350 and 400 °C.

350 °C: CH_4 yield increases from 30 to 65%, whereas CO yield decreases from 4 to 0.4%. In line with characterization results, the better catalytic performance observed in lanthana containing catalyst is related to a higher amount of active sites where CO_2 can be adsorbed, dissociated and then hydrogenated to methane, according to dissociative mechanism [37]. Moreover, according to Wierzbicki et al. [7,47], lanthanum addition not only provides new medium strength basic sites, but also modifies Ni properties enhancing its CO_2 adsorption capacity. Therefore, it can be concluded that La_2O_3 addition clearly promotes the CO_2 conversion and the CH_4 yield.

Activity comparison between catalysts prepared in this work with others recently reported in literature is shown in Table 5 [8,9,27,47]. In general, it can be observed that the addition of a promoter enhances notably the catalytic activity for each formulation. For instance, the addition of V_2O_5 to Ni/ Al_2O_3 catalysts improves considerably nickel dispersion and prevents coke deposition [8], whereas CeO_2 impregnation on Ni/MCM-41 catalyst results in additional CO_2 activation leading to higher conversion [9]. I. Graça et al. studied the performance of a formulation analogous to ours, using CeO_2 (redox promoter) instead of La_2O_3 (structural promoter) and Y zeolite instead of BETA zeolite. It can be observed that activity of the promoted catalysts (14Ni-7Ce/USY and 10Ni-10 La_2O_3 /Na-BETA) is similar, being slightly lower for 14Ni-7Ce/USY catalyst due to a smaller spatial time (W/F_{A_0}).

Finally, the stability of the most active catalyst was evaluated after 24 h on stream at 350 °C (see Fig. 14). Note that CO_2 conversion decreases slightly with time. This deactivation could be related to both active site sintering and coke formation. The second hypothesis was dismissed carrying out a thermo-gravimetric test in 5% O_2 /He of the aged catalyst according to which no relevant loss of mass was observed related to coke oxidation (Fig. S4). After 10h-on-stream, anyway, it seems that catalytic activity remains quite stable since similar CO_2 conversions are observed. In addition, the catalyst is very stable in terms of selectivity: non decrease in CH_4 selectivity is observed after 24 h on stream.

4. Conclusions

The catalytic performance of Y- and BETA-zeolites supported Ni catalysts for CO_2 methanation has been compared and additionally, the effect of La_2O_3 addition as promoter has been evaluated.

The reducibility and dispersion of Ni species play an important role in CO_2 methanation: the higher the value of these properties, the better the catalytic performance. Ni is more dispersed in the form of NiO and Ni^{2+} species on H-Y than on H-BETA due to its higher crystallinity and a more accessible framework. However, the reducibility of Ni is higher in the Ni/H-BETA than in the Ni/H-Y catalyst due to a major proportion of NiO species located on the outer surface of the catalyst. After reduction at 500 °C, H-BETA zeolite supported Ni catalysts present a higher surface of reduced nickel (the active phase for CO_2 methanation) and hence, this leads to a superior activity and selectivity. Neutralization of both Y- and BETA-zeolites by addition of exchanged Na^+ improves the catalytic performance (T_{50} decreases in 30 and 15 °C, respectively). This enhancement is not only due to a greater reducibility, but also to the generation of some weak basicity that improves CO_2 adsorption over the zeolite. Although not big differences in CO_2 conversions are observed comparing Ni/Na-Y and Ni/Na-BETA catalysts, the latter achieves more selectivity towards CH_4 than Ni/Na-Y. Therefore, it can be concluded that Ni/Na-BETA is the best catalyst among those here studied to efficiently carry out the hydrogenation of CO_2 into methane.

According to the physicochemical properties of the samples, the addition of increasing loadings of La_2O_3 to Ni-zeolite catalysts promotes dispersion into smaller Ni particles and improves the CO_2 adsorption capacity of the zeolite. These enhancements in the surface basicity and the Ni dispersion provide a greater amount of both basic and active sites, over which CO_2 can be adsorbed and then hydrogenated into CH_4 .

Table 5

Comparison between the activity results achieved by the prepared Ni/BETA catalysts and by those (unpromoted and promoted) reported in literature by other authors.

Catalyst ^a	Total flow cm ³ ·min ⁻¹	Feed ratio (H ₂ /CO ₂ /Inert)	GHSV (h ⁻¹)	W/FA ₀ (g _{cat} ·h·mol ⁻¹)	X _{CO2} at 350 °C (%)	S _{CH4} at 350 °C (%)	Ref.
20NiO/Al ₂ O ₃	150	12/3/5	n.a.	1.7	42	97	[8]
20NiO-5V ₂ O ₅ /Al ₂ O ₃	150	12/3/5	n.a.	1.7	76	> 99	[8]
15Ni/MCM-41	250	36/9/10	15000	1.6	50	95	[9]
15Ce-15Ni/MCM-41	250	36/9/10	15000	1.6	60	97	[9]
15Ni-HT	100	12/3/5	12000	n.a.	74	99	[7]
15Ni2La-HT	100	12/3/5	12000	n.a.	78	98	[7]
14Ni/USY	250	36/9/10	43000	1.6	42	93	[27]
14Ni-7Ce/USY	250	36/9/10	43000	1.6	57	> 95	[27]
10Ni/Na-BETA	250	16/4/5	10000	4.7	33	88	This work
10Ni-10La ₂ O ₃ /Na-BETA	250	16/4/5	10000	4.7	65	99	This work

^a HT = hydrotalcite; MCM-41 = mesostructured silica; USY = ultra-stable Y.

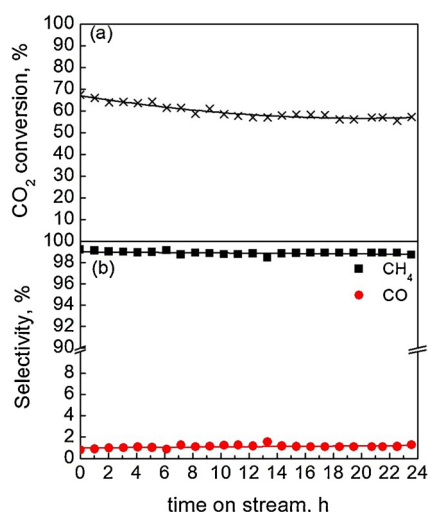


Fig. 14. Evolution of (a) CO₂ conversion and (b) selectivity to CH₄/CO, with time-on-stream over 24 h for Ni-10La₂O₃/Na-BETA catalyst.

In fact, double CO₂ conversion with eventually total selectivity towards CH₄ can be achieved especially at low and intermediate temperatures with Ni-10La₂O₃/Na-BETA, which results in the optimal composition. In contrast, higher loading than 10% La₂O₃ do not achieve additional enhancement of the catalytic performance, since detrimental of the textural properties exceeds the beneficial effect of CO₂ adsorption and hydrogenation sites. After 24 h on stream, this formulation has proven to be quite stable in terms of activity and selectivity.

Acknowledgements

The support from the Economy and Competitiveness Spanish Ministry (CTQ2009-12517 and CTQ2015-67597 MINECO-FEDER) and the Basque Government (IT657-13) and the SGIker (Analytical Services) at the University of the Basque Country are acknowledged. One of the authors (AQ) also acknowledges University of the Basque Country by his PhD grant (PIF-15/351).

Appendix A. Supplementary data

Supplementary material related to this article can be found, in the online version, at doi:<https://doi.org/10.1016/j.apcatb.2018.07.034>.

References

- [1] International Energy Agency, World Energy Outlook 2017, IEA, Paris, 2017 Nov. 14.
- [2] G. Centi, S. Perathoner, CO₂-based energy vectors for the storage of solar energy, Greenhouse Gas Sci. Technol. 1 (2011) 21–35.
- [3] G.A. Nahar, S.S. Madhani, Thermodynamics of hydrogen production by the steam reforming of butanol: analysis of inorganic gases and light hydrocarbons, Int. J. Hydrogen Energy 35 (2010) 98–109.
- [4] J. Gao, Y. Wang, Y. Ping, D. Hu, G. Xu, F. Gu, F. Su, A thermodynamic analysis of methanation reactions of carbon oxides for the production of synthetic natural gas, RSC Adv. 2 (2012) 2358–2368.
- [5] X. Lu, F. Gu, Q. Liu, J. Gao, Y. Liu, H. Li, L. Jia, G. Xu, Z. Zhong, F. Su, VO_x promoted Ni catalysts supported on the modified bentonite for CO and CO₂ methanation, Fuel Process. Technol. 135 (2015) 34–46.
- [6] S. Abate, C. Mebrahtu, E. Giglio, F. Deorsola, S. Bensaid, S. Perathoner, R. Pirone, G. Centi, Catalytic performance of γ-Al₂O₃-ZrO₂-TiO₂-CeO₂ composite oxide supported Ni-based catalysts for CO₂ methanation, Ind. Eng. Chem. Res. 55 (2016) 4451–4460.
- [7] D. Wierzbicki, R. Debek, M. Motak, T. Grzybek, M.E. Gálvez, P. Da Costa, Novel Ni-La-hydrotalcite derived catalysts for CO₂ methanation, Catal. Commun. 83 (2016) 5–8.
- [8] Q. Liu, F. Gu, X. Lu, Y. Liu, H. Li, Z. Zhong, G. Xu, F. Su, Enhanced catalytic performances of Ni/Al₂O₃ catalyst via addition of V₂O₅ for CO methanation, Appl. Catal. A Gen. 488 (2014) 37–47.
- [9] M.C. Bacariza, I. Graça, S.S. Bebian, J.M. Lopes, C. Henriques, Micro- and mesoporous supports for CO₂ methanation catalysts: a comparison between SBA-15, MCM-41 and USY zeolite, Chem. Eng. Sci. 175 (2018) 72–83.
- [10] J. Xu, X. Su, H. Duan, B. Hou, Q. Lin, X. Liu, X. Pan, G. Pei, H. Geng, Y. Huang, T. Zhang, Influence of pretreatment temperature on catalytic performance of rutile TiO₂-supported ruthenium catalyst in CO₂ methanation, J. Catal. 333 (2016) 227–237.
- [11] H. Takano, Y. Kiriha, K. Izumiya, N. Kumagai, H. Habazaki, K. Hashimoto, Highly active Ni/Y-doped ZrO₂ catalysts for CO₂ methanation, Appl. Surf. Sci. 388 (2016) 653–663.
- [12] F. Wang, S. He, H. Chen, B. Wang, L. Zheng, M. Wei, D.G. Evans, X. Duan, Active site dependent reaction mechanism over Ru/CeO₂ catalyst toward CO₂ methanation, J. Am. Chem. Soc. 138 (2016) 6298–6305.
- [13] F. Ocampo, B. Louis, L. Kiwi-Minsker, A.C. Roger, Effect of Ce/Zr composition and noble metal promotion on nickel based Ce_xZr_{1-x}O₂ catalysts for carbon dioxide methanation, Appl. Catal. A Gen. 392 (2011) 36–44.
- [14] David J. Elliott, J.H. Lunsford, Kinetics of the methanation reaction over Ru, Ru-Ni, Ru-Cu and Ni clusters in zeolite Y, J. Catal. 57 (1979) 11–26.
- [15] N.C. Saha, E.E. Wolf, CO methanation activity and XPS studies of Pd supported on ZSM5 and Y-zeolites, Appl. Catal. A Gen. 13 (1984) 101–112.
- [16] V. Patzelová, A. Zukal, Z. Tvaruzková, O. Malicek, Hydrogenation of CO and CO₂ over stabilized NiY catalysts, Stud. Surf. Sci. Catal. 18 (1984) 367–374.
- [17] J. Weitkamp, M. Hunger, U. Ryma, Base catalysis on microporous and mesoporous materials: recent progress and perspectives, Microporous Mesoporous Mater. 48 (2001) 255–270.
- [18] K.S. Walton, M.B. Abney, M.D. LeVan, CO₂ adsorption in Y and X zeolites modified by alkali metal cation exchange, Microporous Mesoporous Mater. 91 (2006) 78–84.
- [19] S.T. Yang, J. Kim, W.S. Ahn, CO₂ adsorption over ion-exchanged zeolite beta with alkali and alkaline earth metal ions, Microporous Mesoporous Mater. 135 (2010) 90–94.
- [20] P. Concepción-Heydorn, C. Jia, D. Herein, N. Pfänder, H.G. Karge, F.C. Jentoft, Structural and catalytic properties of sodium and cesium exchanged X and Y zeolites, and germanium-substituted X zeolite, J. Mol. Catal. A: Chem. 162 (2000) 227–246.
- [21] M.C. Bacariza, R. Bértolo, I. Graça, J.M. Lopes, C. Henriques, The effect of the compensating cation on the catalytic performances of Ni/USY zeolites towards CO₂ methanation, J. CO₂ Util. 21 (2017) 280–291.
- [22] A.N. Pinheiro, A. Valentini, J.M. Sasaki, A.C. Oliveira, Highly stable dealuminated zeolite support for the production of hydrogen by dry reforming of methane, Appl. Catal. A Gen. 355 (2009) 156–168.
- [23] G. Nareish, V.V. Kumar, Ch. Anjaneyulu, J. Tardio, S.K. Bhargava, J. Patel, A. Venugopal, Nano size Hβ zeolite as an effective support for Ni and Ni-Cu for CO_x free hydrogen production by catalytic decomposition of methane, Int. J. Hydrogen Energy 41 (2016) 19855–19862.
- [24] J. Dědeček, L. Čapek, D. Kaucký, Z. Sobalík, B. Wichterlová, Siting and distribution of the Co ions in beta zeolite: a UV-Vis-NIR and FTIR study, J. Catal. 211 (2002)

- 198–207.
- [25] A. Srebowata, R. Baran, D. Lomot, D.L. Lisovyt'skiy, T. Onfroy, S. Dzwigaj, Remarkable effect of postsynthesis preparation procedures on catalytic properties of Ni-loaded BEA zeolites in hydrodechlorination of 1,2-dichloroethane, *Appl. Catal. B* 147 (2014) 208–220.
 - [26] A. Srebowata, I. Zielinska, R. Baran, G. Slowik, S. Dzwigaj, Ag-Ni bimetallic SiBEA zeolite as an efficient catalyst of hydrodechlorination of 1,2-dichloroethane towards ethylene, *Catal. Commun.* 69 (2015) 154–160.
 - [27] I. Graça, L.V. González, M.C. Bacariza, A. Fernandes, C. Henriques, J.M. Lopes, M.F. Ribeiro, CO₂ hydrogenation into CH₄ on NiHNaUSY zeolites, *Appl. Catal. B* 147 (2014) 101–110.
 - [28] M.C. Bacariza, I. Graça, A. Westermann, M.F. Ribeiro, J.M. Lopes, C. Henriques, CO₂ hydrogenation over Ni-based zeolites: effect of catalysts preparation and pre-reduction conditions on methanation performance, *Top. Catal.* 59 (2016) 314–325.
 - [29] Z. Boukha, C. Jiménez-González, B. de Rivas, J.R. González-Velasco, J.I. Gutiérrez-Ortiz, R. López-Fonseca, Synthesis, characterization and performance evaluation of spinel-derived Ni/Al₂O₃ catalysts for various methane reforming reactions, *Appl. Catal. B* 158–159 (2014) 190–201.
 - [30] M. Suzuki, K. Tsutsumi, H. Takahashi, Y. Saito, T.p.r. study on reducibility of nickel ions in zeolite Y, *Zeolites* 9 (1989) 98–103.
 - [31] A. Luengnaruemitchai, A. Kaengsilalai, Activity of different zeolite-supported Ni catalysts for methane reforming with carbon dioxide, *Chem. Eng. J.* 144 (2008) 96–102.
 - [32] J. Aguado, D.P. Serrano, J.M. Escola, L. Briones, Deactivation and regeneration of a Ni supported hierarchical Beta zeolite catalyst used in the hydrotreating of the oil produced by LDPE thermal cracking, *Fuel* 109 (2013) 679–686.
 - [33] D.P. Serrano, J.M. Escola, L. Briones, S. Medina, A. Martínez, Hydrotreating of the oils from LDPE thermal cracking over Ni-Ru and Ru supported over hierarchical Beta zeolite, *Fuel* 144 (2015) 287–294.
 - [34] P.M. Lima, T. Garetto, C.L. Gavalcane Jr, D. Cardoso, Isomerization of n-hexane on Pt-Ni catalysts supported on nanocrystalline H-BEA zeolite, *Catal. Today* 172 (2011) 195–202.
 - [35] T. Lehmann, T. Wolff, C. Hamel, P. Veit, B. Garke, A. Seidel-Morgenstern, Physico-chemical characterization of Ni/MCM-41 synthesized by a template ion exchange approach, *Microporous Mesoporous Mater.* 151 (2012) 113–125.
 - [36] Z. Zheng, C. Sun, R. Dai, S. Wang, X. Wu, X. An, Z. Wu, X. Xie, Ethanol steam reforming on Ni-based catalysts: effect of Cu and Fe addition on the catalytic activity and resistance to deactivation, *Energy Fuels* 31 (2017) 3091–3100.
 - [37] J. Ren, H. Guo, J. Yang, Z. Qin, J. Lin, Z. Liu, Insights into the mechanisms of CO₂ methanation on Ni(111) surfaces by density functional theory, *Appl. Surf. Sci.* 351 (2015) 504–516.
 - [38] Y. Cui, H. Zhang, H. Xu, W. Li, The CO₂ reforming of CH₄ over Ni/La₂O₃/α-Al₂O₃ catalysts: the effect of La₂O₃ contents on the kinetic performance, *Appl. Catal. A Gen.* 331 (2007) 60–69.
 - [39] W. Ahmad, M. Naeem Younis, R. Shawabkeh, S. Ahmed, Synthesis of lanthanide series (La, Ce, Pr, Eu & Gd) promoted Ni/γ-Al₂O₃ catalysts for methanation of CO₂ at low temperature under atmospheric pressure, *Catal. Commun.* 100 (2017) 121–126.
 - [40] B. Pawelec, R. Mariscal, R.M. Navarro, J.M. Campos-Martin, J.L.G. Fierro, Simultaneous 1-pentene hydroisomerization and thiophene hydrodesulphurization over sulphided Ni/FAU and Ni/ZSM-5 catalysts, *Appl. Catal. A Gen.* 262 (2004) 155–166.
 - [41] Z. Boukha, L. Fitian, M. López-Haro, M. Mora, J. Rafael Ruiz, C. Jiménez-Sanchidrián, G. Blanco, J.J. Calvino, G.A. Cifredo, S. Trasobares, S. Bernal, Influence of the calcination temperature on the nano-structural properties, surface basicity, and catalytic behaviour of alumina-supported lanthana samples, *J. Catal.* 272 (2010) 121–130.
 - [42] Q. Pan, J. Peng, T. Sun, S. Wang, S. Wang, Insight into the reaction route of CO₂ methanation: promotion effect of medium basic sites, *Catal. Commun.* 45 (2014) 74–78.
 - [43] A.S. Al-Fatesh, M.A. Naeem, A.H. Fakeeha, A.E. Abasaheed, Role of La₂O₃ as promoter and support in Ni/γ-Al₂O₃ catalysts for dry reforming of methane, *Chin. J. Chem. Eng.* 22 (1) (2014) 28–37.
 - [44] R. Yang, C. Xing, C. Lv, L. Shi, N. Tsubaki, Promotional effect of La₂O₃ and CeO₂ on Ni/γ-Al₂O₃ catalysts for CO₂ reforming of CH₄, *Appl. Catal. A Gen.* 385 (2010) 92–100.
 - [45] H.W. Kim, K.-M. Kang, H.-Y. Kwak, J.H. Ki, Preparation of supported Ni catalysts on various metal oxides with core/shell structures and their tests for the steam reforming of methane, *Chem. Eng. J.* 168 (2011) 775–783.
 - [46] M.I. Alymov, N.M. Rubtsov, B.S. Seplyarskii, R.A. Kochetkov, V.A. Zelensky, B. Ankudinov, Combustion and passivation of nickel nanoparticles, *Mendeleev Commun.* 27 (2017) 631–633.
 - [47] D. Wierzbicki, R. Baran, R. Debek, M. Motak, M.E. Gálvez, T. Grzybek, P. Da Costa, P. Glatzel, Examination of the influence of La promotion on Ni state in hydrotalcite derived catalysts under CO₂ methanation reaction conditions: operando X-ray absorption and emission spectroscopy investigation, *Appl. Catal. B* 232 (2018) 409–419.